UltraRapid Communication

A Computer Model of Normal Conduction in the Human Atria

David M. Harrild, Craig S. Henriquez

Abstract—Although considerable progress has been made in understanding the process of wavefront propagation and arrhythmogenesis in human atria, technical concerns and issues of patient safety have limited experimental investigations. The present work describes a finite volume–based computer model of human atrial activation and current flow to complement these studies. Unlike previous representations, the model is three-dimensional, incorporating both the left and right atria and the major muscle bundles of the atria, including the crista terminalis, pectinate muscles, limbus of the fossa ovalis, and Bachmann's bundle. The bundles are represented as anisotropic structures with fiber directions aligned with the bundle axes. Conductivities are assigned to the model to give realistic local conduction velocities within the bundles and bulk tissue. Results from simulations demonstrate the role of the bundles in a normal sinus rhythm and also reveal the patterns of activation in the septum, where experimental mapping has been extremely challenging. To validate the model, the simulated normal activation sequence and conduction velocities at various locations are compared with experimental observations and data. The model is also used to investigate paced activation, and a mechanism of the relative lengthening of left versus right stimulation is presented. Owing to both the realistic geometry and the bundle structures, the model can be used for further analysis of the normal activation sequence and to examine abnormal conduction, including flutter. The full text of this article is available at http://www.circresaha.org. **(*Circ Res*. 2000;87:e25-e36.)**

Key Words: atrial computer model ■ cardiac propagation ■ atrial conduction ■ finite volume method

Atrial arrhythmias are electrical disturbances in the heart that can range in severity from annoying to life-threatening. The process of understanding these malformed rhythms must begin with a thorough comprehension of the normal spread of activation in the human heart. Experimental techniques, including recordings with microelectrodes[1] and single[2] or multiple[3,4] extracellular electrodes, have yielded a wealth of information. Each technique, however, is associated with its own set of complications and limitations, exacerbated by the complexity of the atrial anatomical architecture.[5,6]

Meanwhile, and in parallel with experimental studies, a number of computer models of atrial conduction have been described. Briefly, they began with the important cellular automaton of Moe et al.[7] Later, isotropic cellular automata include descriptions by Macchi[8] (later modified by Kafer[9]), Lorange and Gulrajani,[10] Wei et al,[11] and Killmann et al.[12] Several atrial models have used realistic membrane kinetics. Winslow et al described a flat, isotropic 2D sheet with an Earm and Noble[13] membrane. Virag et al[14] represented the atria by folding a 2D sheet in space and penetrating it with a series of holes; they used Luo-Rudy I[15] kinetics. Recent reports have also emerged of modeled activity in a single 1D pectinate muscle attached to an underlying rectangular sheet.[16,17]

In this article, we present the first membrane-based model of 3D conduction in a realistic human atrial geometry. The model includes both the left and right atria, including representations of the major atrial bundles and a right-sided endocardial network of pectinate muscles. The membrane's kinetics are governed by the Nygren et al[18] formulation for the human atrial cell. Because a simulation of wavefront conduction in a model of the atria with this degree of complexity has not heretofore been undertaken, the goals of this study are (1) to perform a comprehensive validation by comparing simulated patterns of activation and location conduction velocities during normal sinus rhythm and left/right pacing with published experimental observations and data and (2) to investigate the role of the well-defined atrial bundles in establishing the global activation sequence. The model provides a unique view of atrial activation, particularly in regions that cannot be easily recorded in patients. Consequently, activation maps are displayed in a 3D representation, avoiding the distortion that can arise from projecting 3D data onto a 2D surface.[19] Although the focus of this work is on normal activation, the model provides a framework in which to easily conduct computer-based investigations of macroscopic atrial conduction, both normal and abnormal.

Received July 7, 2000; revision received September 11, 2000; accepted September 11, 2000.

From the Department of Biomedical Engineering, Duke University, Durham NC.

Correspondence to Craig S. Henriquez, Box 90281, Department of Biomedical Engineering, Duke University, Durham NC 27708-0281. E-mail ch@duke.edu

Circulation Research **is available at http://www.circresaha.org**

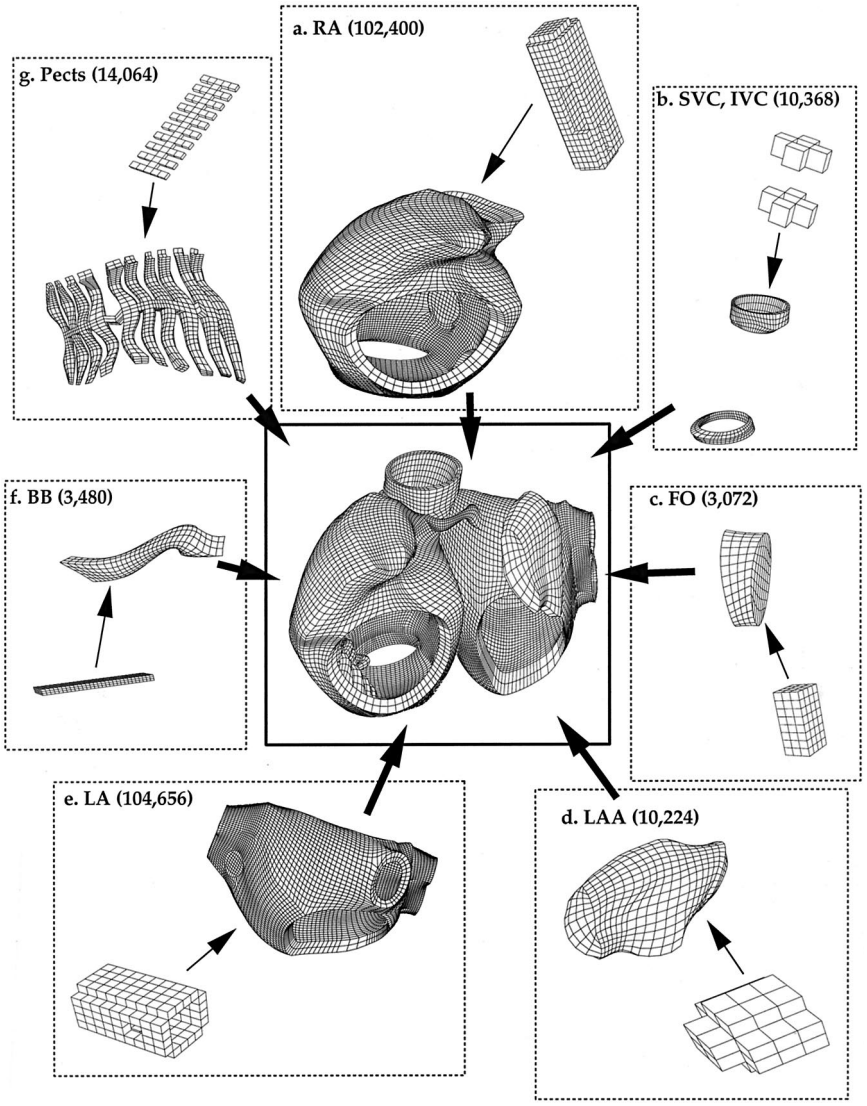

Figure 1. Block structure and low-density mesh views of each of the 7 parts (a through g) (periphery) and the fully assembled mesh (center). The number of elements used for each of the parts is indicated. The complete mesh includes 248 264 hexahedral elements. RA indicates right atrium; SVC/IVC, superior/inferior vena cava; FO, interatrial connection at the fossa ovalis; LAA, left atrial appendage; LA, left atrium; BB, Bachmann's bundle; and Pects, pectinate muscles.

Materials and Methods

Anatomy of the Atrial Mesh

We have constructed a boundary-conforming mesh of the human atria comprised entirely of hexahedral (eg, 6-sided) elements. The original set of surfaces used to guide the creation of the mesh was purchased from Viewpoint Digital. These surfaces were compared with literature reports of normal human atrial dimensions[20–30]; where they diverged from these, they were modified accordingly. The dimensions of components of the mesh are given in supplemental Tables 1 through 3 (available in an online data supplement at http://www.circresaha.org). From the modified surfaces, a block-structured (multiblock) hexahedral mesh[31,32] was made using TrueGrid from XYZ Scientific Applications.

The assembled human atrial mesh is presented in the center panel of Figure 1, in a left anterior view (see supplemental animation, spinning_mesh.mpg; available in an online data supplement at http://www.circresaha.org). The mesh includes 248,264 elements and is comprised of 7 constituent parts, each of which appears in the periphery of Figure 1. The block structure of each part appears in Figure 1, at the beginning of the chain of arrows leading to the full mesh. Figure 2 shows the left anterior (a) and posterior (b) views of the surface-rendered complete mesh. A detailed view of the right atrial endocardial structure appears in Figure 3. Two interatrial connections, Bachmann's bundle and a region at the fossa ovalis (Figure 4d), carry current between the right and left atria. A number of meshed regions are defined to be bundles. These regions are the crista terminalis; the right atrial pectinate muscle network; Bachmann's bundle; the intercaval bundle; and the limbus of the fossa ovalis (Figures 4a and 4b). The number of elements used in each component part of the mesh is scalable. The mesh used for simulations had element sizes that ranged from 50 to 1650 μm, with a mean interelement distance of 550 μm; 95% of the step sizes are smaller than 1060 μm. Most of the largest elements were located in the left atrial appendage.

Current Flow

The mathematics of the monodomain model and finite volume method used to model the spatial spread of electric current has been described by us previously.[33] The transmembrane flow is represented according to the human atrial cell formulation of Nygren et al.[18] The cell diameter listed by them of 11 μm gives rise to a surface-to-volume ratio of 3636/cm in our model.

Assignment of Regional Conductivities

To minimize complexity, only 3 conductivities are assigned to the model. The values of conductivities were selected to obtain realistic conduction velocities of $\approx$60 to 75 cm/s in the bulk tissue, 150 to 200 cm/s in the bundles, and 30 to 40 cm/s in slow regions.

Because the model of Nygren et al[18] assumes a surface-to-volume ratio of 3636/cm and produces a propagating action potential with a

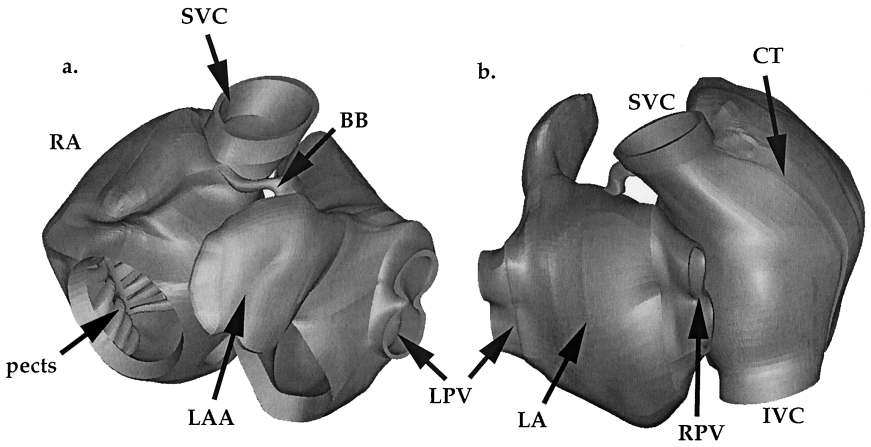

Figure 2. Left anterior (a) and posterior (b) views of the complete atrial model. SVC indicates superior vena cava; IVC, inferior vena cava; RA, right atrium; LA, left atrium; LAA, left atrial appendage; R/LPV, right/left pulmonary veins; pects, pectinate muscle network; BB, Bachmann's bundle; and CT, crista terminalis.

relatively slow upstroke rate of rise of 110 V/s, it was necessary to assign a high conductivity of 12.02 mS/cm to the bulk tissues to obtain realistic wavespeeds. To implement fast propagation in the longitudinal direction of the bundles, the conductivity along the bundle axes is increased to 90.70 mS/cm; the transverse component was the same as the bulk value. Slow isotropic conduction is assigned to 2 regions, illustrated in Figure 4c. The first, the isthmus of the right atrial floor, is a region of known slow conduction.[34–36] The isotropic assumption here is a known simplification of the structural reality. The interatrial connection at the fossa ovalis is the other slow region, a reflection of the discordant activation of the right and left atrial septa.[37,38] The conductivity in these regions is 3.63 mS/cm. From 1D analysis, the ratio of the conduction velocities in the fast and slow tissue, relative to the bulk tissue, for the given conductivities should be 2.75 and 0.55 (given by the square root of the conductivities[39]). Differences from these values at specific locations in the atria arise as a consequence of the influence of geometry on the global conduction patterns.

Numerical Issues

The application of the finite volume method to the block-structured grid gives rise to a sparse, symmetric positive–definite matrix. The Cuthill-McGee algorithm was applied to reduce the matrix bandwidth. A table-lookup for some of the rate constants in the Nygren et al[18] model was used to accelerate the calculations. A first-order, semi-implicit time integration scheme was used with a fixed time step of 20 μs. The system of equations was solved iteratively using the conjugate gradient method with a convergence tolerance of 10^{-6}. A simulation of 125 ms of activation required 115 minutes of CPU

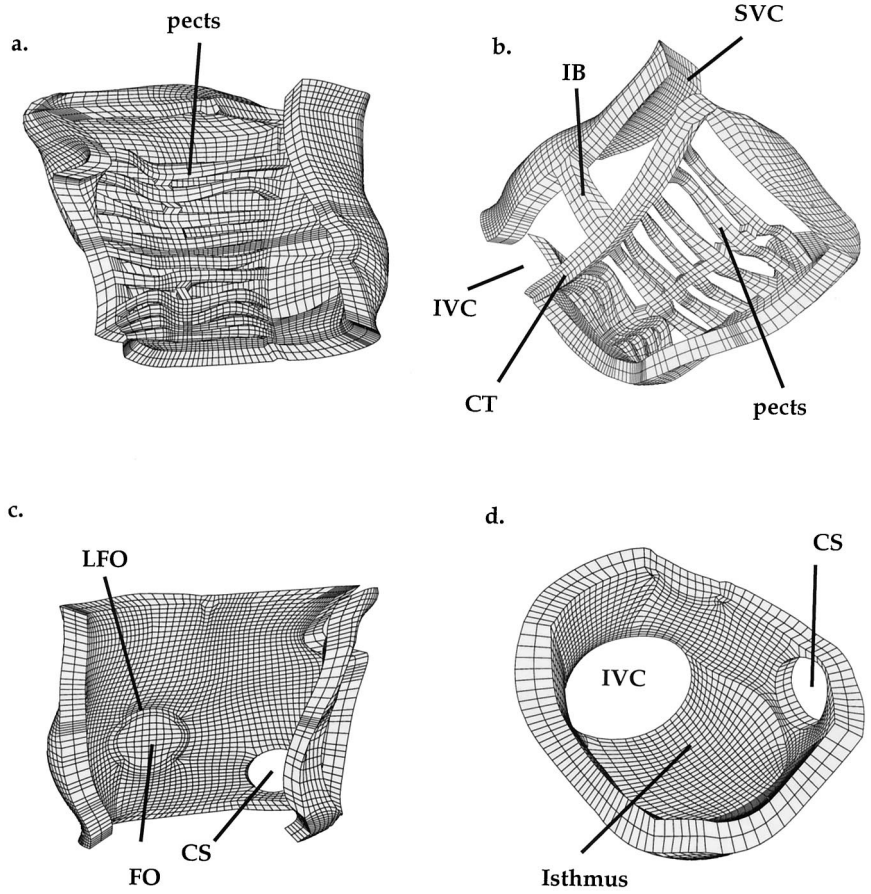

Figure 3. View of the right atrial endocardial structure. Highlighted structures include the pectinates (pects), crista terminalis (CT), fossa ovalis (FO), coronary sinus (CS), limbus of the fossa ovalis (LFO), superior/inferior vena cava (SVC/IVC), and intercaval bundle (IB).

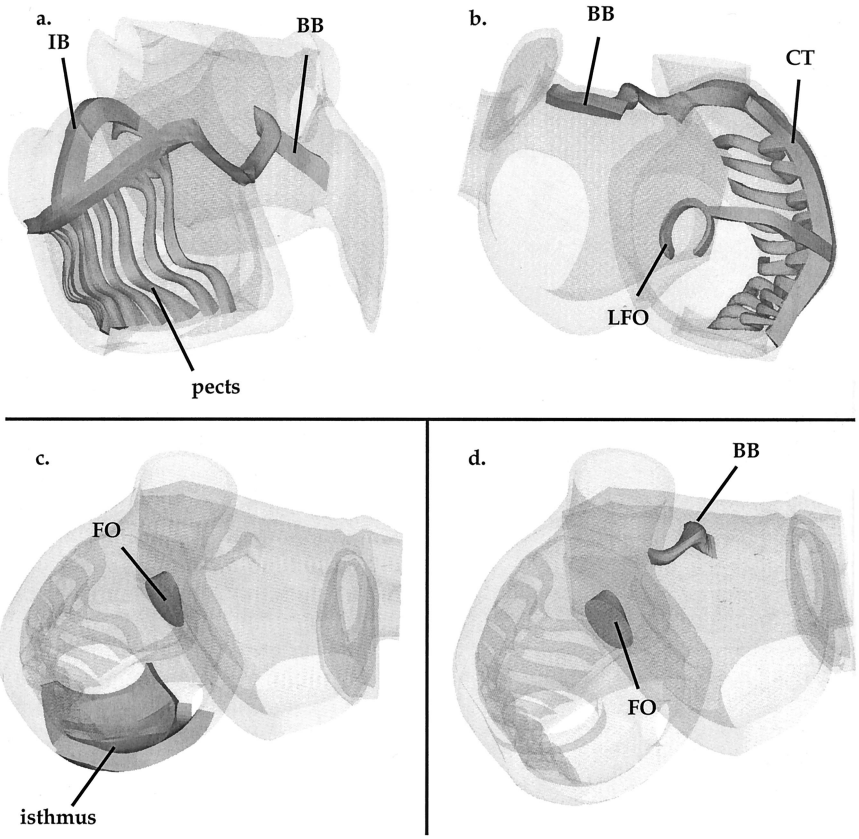

Figure 4. Muscle bundles contained within the model with fast anisotropic conduction. Views are superolateral (a) and posterior (b). c, Regions of the model with slow conduction. d, Two interatrial connections in the model, in their anatomic position. IB indicates intercaval bundle; BB, Bachmann's bundle; pects, pectinate muscles; LFO, limbus of fossa ovalis; and FO, interatrial connection at the fossa ovalis.

time on 28 processors on an IBM SP (Power 3, 200 MHz) at the North Carolina Supercomputing Center (Research Triangle Park, NC).

Although a complete convergence study on the effect of the spatial step sizes on the solution for the whole mesh was not possible owing to computational limitations, an analysis of a section of the right atrial free wall showed that increasing the density of elements from 27 440 to 92 610 (150% as dense in each direction) had a negligible effect on the activation pattern and total activation time (see supplemental Figure 1; available in an online data supplement at http://www.circresaha.org).

Results

Simulation of the Normal Activation Sequence in Human Atria

A simulation was performed to analyze the global conduction pattern in the model resulting from assigning a higher conductivity in the bundles than in the bulk tissue to represent the faster local conduction velocity. Figure 5 shows a number of snapshots of the progression of the expanding wavefront (color version, supplemental Figure 2, and supplemental animation, normal_act.mpg; available in an online data supplement at http://www.circresaha.org). In each case, the tissue activated at or before the indicated time is solid; the surrounding inactive tissue is translucent. The color gradient, in each figure, runs from earliest to latest activation for that time step. The capital letters in subsequent text refer to the corresponding letters in the figure.

A stimulus of 2 ms in duration and of sufficient strength to cause the initiation of a propagating wavefront is applied to the sinoatrial (SA) node region and by 10 ms, the wave begins to spread outward. By 20 ms, the wave quickly spreads anterior to the superior vena cava as a consequence of the increased conductivity in the crista arch (A). The anisotropy of the crista in the posterior wall is obvious here; the wavefront becomes nearly triangular as the crista activation precedes, and draws forth, that of the surrounding wall (B). Importantly, also, the depolarizing wave has now begun to spread through the proximal portions of the first 3 pectinate muscles (C). By 30 ms, a large portion of the superior wall has become active, and the excitation begins to descend the septal surface. The wave in the crista has already almost reached the inferior border of the posterior atrium. Almost all of the pectinates are active to some degree; conduction from the middle of the superior few pectinates to the endocardial wall is evident (D). The impulse in the first pectinate is nearing its terminus on the tricuspid rim. Importantly, the depolarizing wave has now traversed the interatrial Bachmann's bundle and has merged with the anterior septal portion of the left atrial wall (E). The first activation of the left atrial surface has occurred just before this snapshot, at 29.7 ms. In the left atrial wall, an elliptic wavefront begins to expand, a reflection of the anisotropy of this bundle.

By 40 ms, the wavefronts have all but encircled the os of the superior vena cava. A more substantial portion of the left atrial wall has become active. Fully half of the pectinates are depolarized throughout; the adjacent muscle at their termini is activated by the impulse traversing these structures just before it is reached by the wave in the free wall proper. Septally, the wave has just reached the second interatrial connection, at the fossa ovalis (F). Ten milliseconds later, the

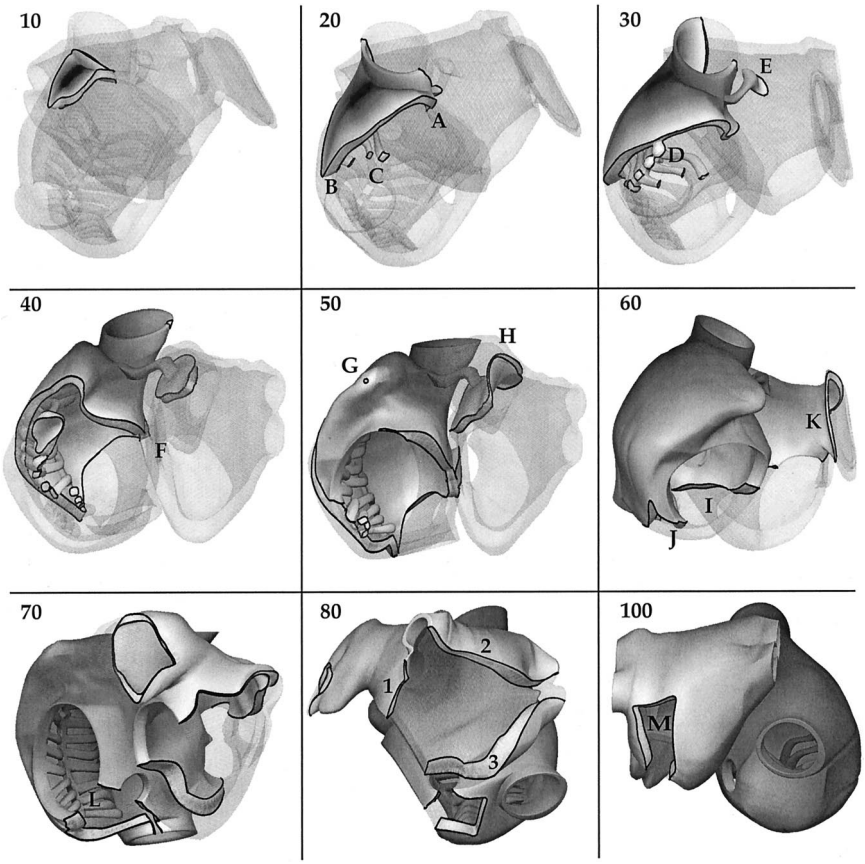

Figure 5. Progression of the normally conducting wavefront. The number in the upper left of each panel indicates the time after stimulation, in ms. For each image, the colors run from blue (minimum) to red (maximum). See the text for specific comments on numbers and letters in the figure.

tip of the right atrial appendage borders on complete activation (G). The impulse has coursed through the entire length of every pectinate. Rapid conduction through Bachmann's bundle in the left atrium has brought the impulse to the mouth of its appendage and has activated a substantial portion of the left atrial superior wall (H). The interatrial connection at the fossa ovalis is largely active. The influence of the posterior crista is still evident in the spiky projection of the wavefront toward this structure's end. The next frame (60 ms) shows the progression of the right atrial septal wave (I), as the annulus of the tricuspid valve becomes increasingly surrounded by active tissue. The floor of the right atrium (J) remains mostly inactive. In the left atrium, the connection at the fossa ovalis has depolarized the region surrounding it (first occurring at about 51.5 ms). The wavefront begins to creep along the medial wall of the appendage (K) and posteriorly in the superior left atrial wall.

By 70 ms, the wave has completely encircled the mouth of the left atrial appendage. The interatrial connection at the fossa ovalis now contributes substantially to left atrial septal activation, and the left atrial anterosuperior wall is completely depolarized. The only portion of the right atrial anatomy that remains unexcited is its floor (L), where conduction proceeds slowly because of the reduced conductivity value there. A shrinking island of right atrial isthmic tissue remains unaffected at 80 ms. The depolarization of the left atrial appendage is now nearly complete. In the left atrium proper, 3 separate wavefronts approach the inferior lateral surface (labeled 1 to 3). Two of these waves, progressing inferiorly (1 and 2), are separated by the left pulmonary veins; the other (3) will advance superiorly. By 100 ms, one notices that the right atrium has been entirely activated (actually occurring at 99.3 ms). (Note that if the slow conduction in the right atrial floor is removed by imposing the bulk conductivity value there, this last activation occurs at 81.2 ms.) A small inactive bridge of tissue, parallelopiped in appearance, abuts the mitral annulus in the lateral inferior left atrium (M). At 108.2 ms, this last remaining portion of tissue becomes active.

Figure 6 presents the entire activation sequence in summary form. Figure 6a highlights the anisotropic conduction along the crista (1). In Figure 6b, note the circle of activation formed around the first point of breakthrough on the right appendage, at the terminus of the first pectinate muscle (2). This panel also presents a view of the point of last activation of the left atrial appendage (3). In Figure 6c, notice the convergence of the three wavefronts to the point of last atrial activation, in the inferior region of the left atrium (4). The closely spaced isolines in the right atrial floor reflect the slow conduction velocity there (5). In Figure 6d, a lateral view of the right atrium is presented, with the free wall and lateral surfaces removed to highlight the activity in the pectinates. The relative paucity of isolines (compared, for example, with the floor visible just below them) serves as an indication of the rapid conduction in these structures. Transverse conduction between pectinates, occurring in a superior-to-inferior fashion, is also apparent (6).

The local conduction velocities measured at a number of points in the model during normal activation are summarized

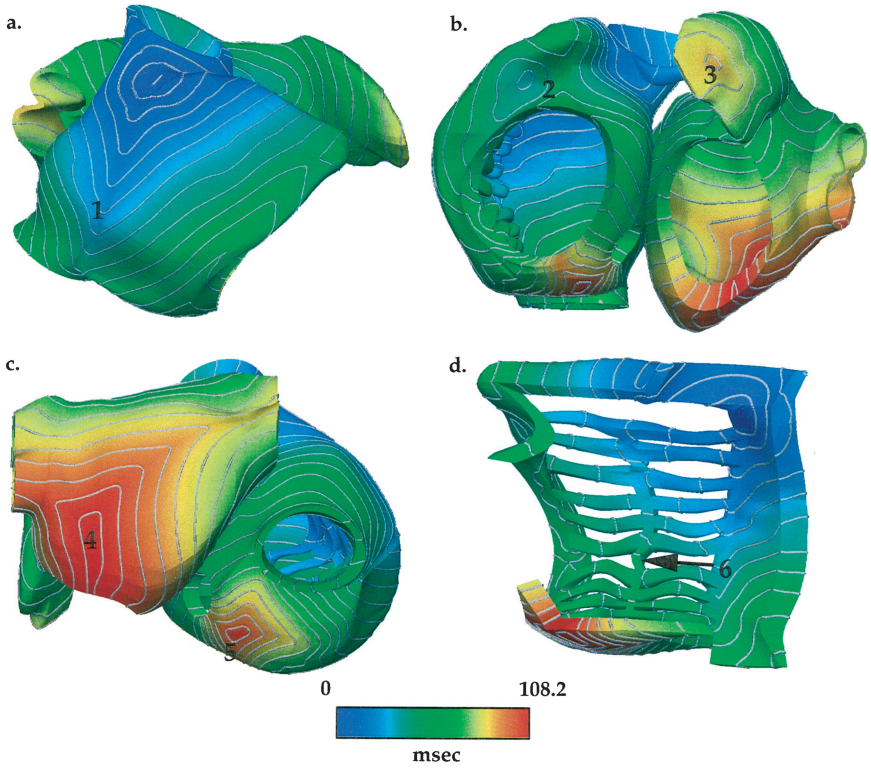

Figure 6. Various views of the mesh, showing the entire sequence of activation (a through c). Isoline spacing is 5.0 ms. d, Free wall and septum of the right atrium have been removed; the view is lateral. See the text for details.

in Figure 7. The velocity in the bulk tissue averages ≈74 cm/s. Within the bundles, the velocities are considerably greater, ranging between 110 and 177 cm/s. The slowest conduction, 40 cm/s, is found in the floor of the right atrium. Note that these velocities do not correspond to those of planar wavefronts but rather reflect the complex pattern of activation, front shape, and, in some regions, collisions of fronts (eg, left atrial appendage) that result naturally from the global activation sequence.

The sequence of activation in the right atrial septum is highlighted in Figure 8a (color version, supplemental Figure 3; available in an online data supplement at http://www.circresaha.org). Excitation progresses broadly in 2 directions, curling posteriorly around the superior vena cava and superiorly within the arch of the crista. The 2 waves collide within the posterior septal wall and accelerate along the fast bundles of the fossa ovalis rim. Traveling inferiorly, the wave becomes quite planar and bends around the os of the coronary sinus, terminating within the slow right atrial isthmus. In the left atrium, the septal activation sequence (Figure 8b) follows as a direct consequence of the right atrial patterns. Breakthrough at Bachmann's bundle conducts anteriorly in an elliptical fashion, a consequence of this structure's anisotropy. Later, conduction through the fossa ovalis region contributes to inferoposterior activation in the septum.

Activation Patterns From Pacing

In Figure 9 (right), a stimulus is applied to the right atrial appendage (color version, supplemental Figure 4, and animation, paced_ra.mpg; available in an online data supplement at http://www.circresaha.org). The early progression of the wavefront is circular. It first reaches the crista by retrograde conduction through the fast pectinate bundles rather than via the slow free wall (1 in Figure 9f). The wavefront, upon reaching the crista, becomes elongated along the axis of this bundle. The time for activation of all the right atrial tissue is ≈116 ms; the last tissue activated is in its floor. The left atrium first becomes active at 44 ms via Bachmann's bundle. The fossa interatrial impulse reaches the left atrium at 74.3 ms. Unlike the right atrial activation pattern, that of the left atrium is essentially normal. The activation of the last left atrial tissue occurs at 127.7 ms and is located at 2 in its posterior inferior region, slightly more lateral than in the normal case.

The conduction pattern resulting from pacing the left atrial appendage is shown in Figure 9 (left) (supplemental animation, paced_la.mpg; available in an online data supplement at http://www.circresaha.org). Leaving the appendage, the wavefront accelerates along the fast Bachmann's bundle in the anterosuperior left atrial wall (3). It proceeds broadly along 3 routes in the left atrium. It courses into the superior wall, delineated by the ora of the pulmonary veins, and anterior to posterior on both sides of the mitral valve orifice. These wavefronts collide first in the posterior lateral wall (4) and, ultimately, in the inferior posterior medial region (5, at 123.0 ms).

The wave first gains entrance to the right atrium at 62.7 ms via Bachmann's bundle. The right atrial fossa ovalis is activated simultaneously by a septal wave progressing inferiorly from Bachmann's bundle and by the left atrial wave traveling across the interatrial connection there. These waves converge at ≈99 ms. At the same time, the wave crests over the superiormost region of the right atrial wall, arriving at the SA node area and crista terminalis at about the same time that it reaches the annulus of the tricuspid valve. An interesting conduction pattern results in the superior pectinates, as waves conduct

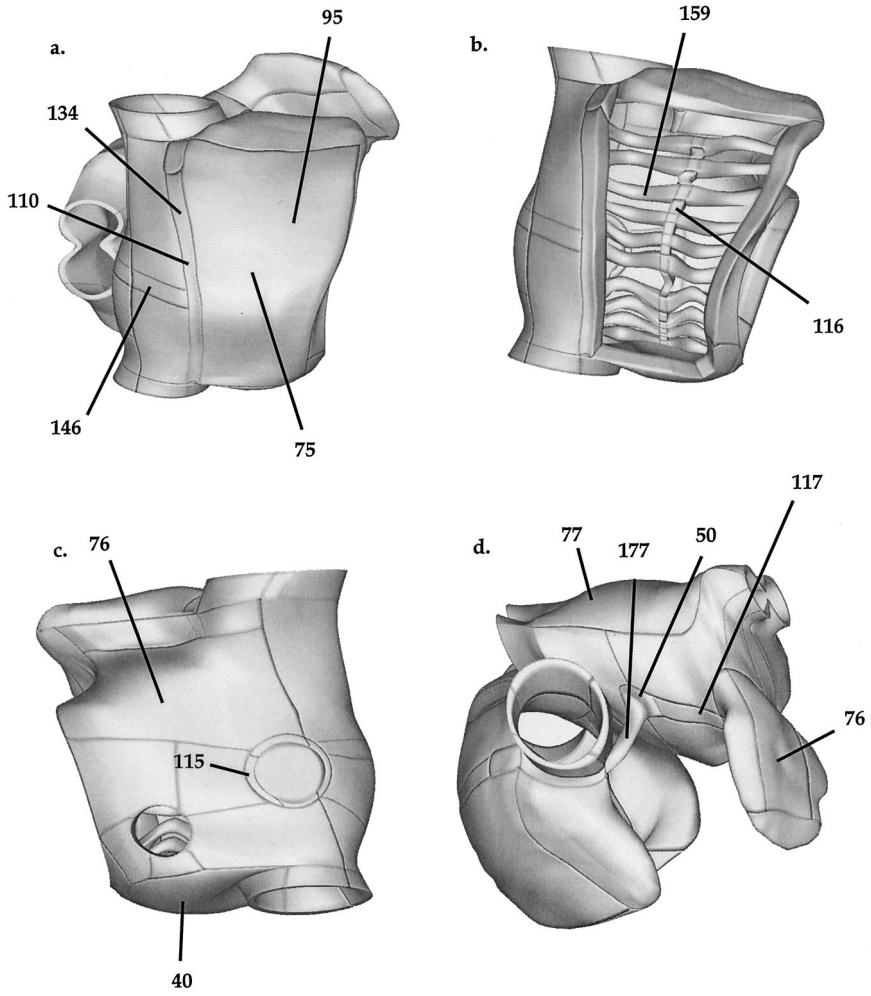

Figure 7. Conduction velocities (cm/s) measured at various points in the model during normal sinus rhythm. A block version is shown to highlight the bundles present therein.

from both of the pectinate ends toward their centers. This configuration is shown at point 6 in Figure 9e, a snapshot of activity taken at 150 ms. The region of last activation remains in the atrial floor, occurring at ≈169 ms; the total time for activation of the right atrium is thus ≈106 ms.

Discussion

It has been asserted that the specifics of atrial anatomy are critically important in determining the spread of the activating wavefront.[6,40] There are a number of well-defined uninsulated bundles in the atrial muscle within which current flow is rapid.[40,41] These bundles include the crista terminalis, the pectinate muscles, Bachmann's bundle, and the limbus of the fossa ovalis.[42] As a consequence, these anatomical features were meshed as discrete structures in our model, and within these bundles, the hexahedral elements are aligned with their longitudinal axes. Their fiber angles could thus be aligned with the bundle axes, critical for the incorporation of anisotropy into the model. Anisotropy is an established and important property of the atrial bundles.[43]

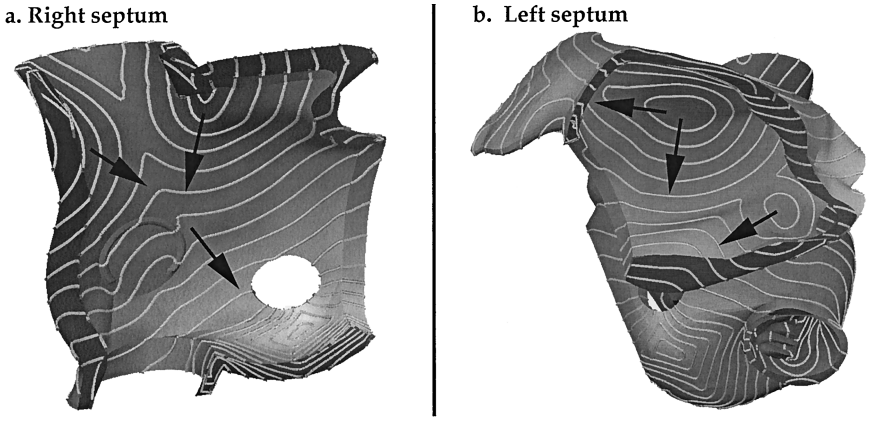

Figure 8. Views of right (a) and left (b) septal conduction. The dual inputs to the left-sided activation are apparent. The arrows indicate the direction of wavefront propagation.

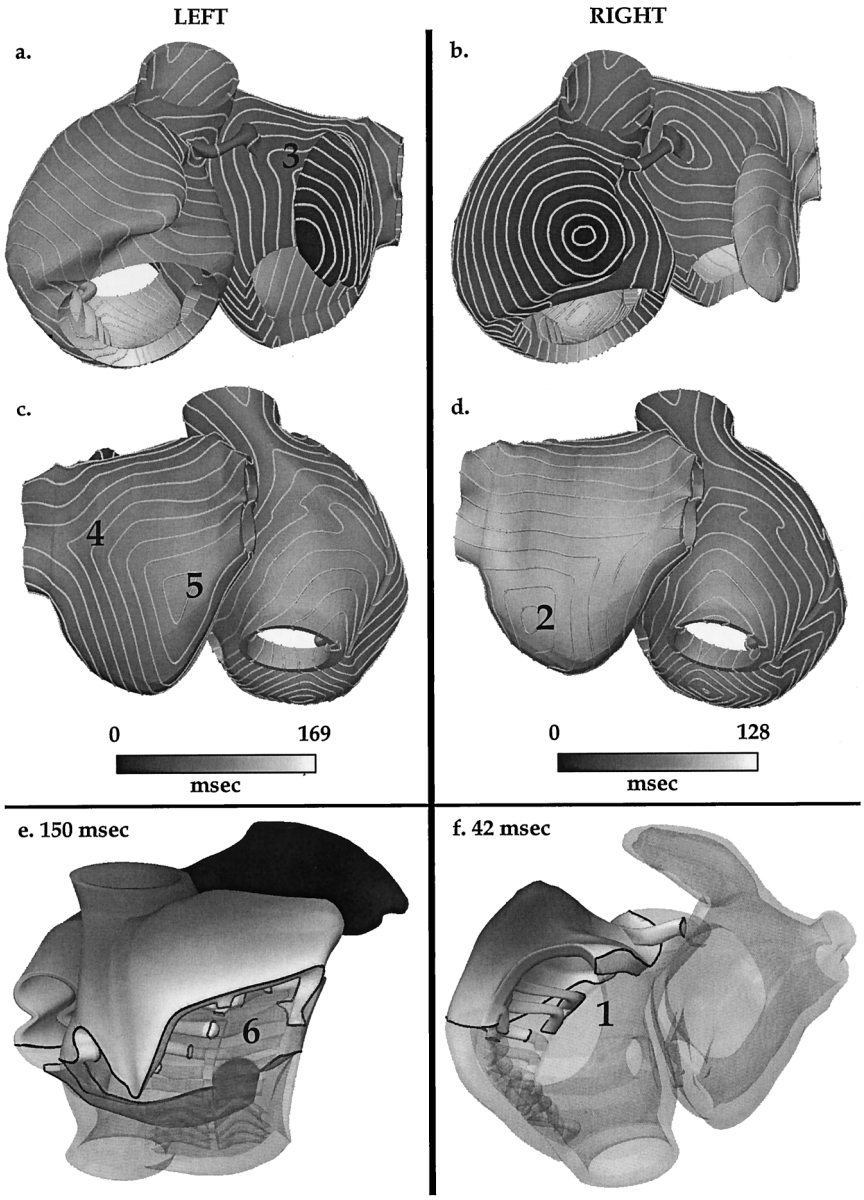

Figure 9. Conduction pattern resulting from the application of a pacing stimulus to the right and left atrial appendages (right and left panels of the figure, respectively). a through d, Views of the overall activation maps (anterosuperior [a and b]; posteroinferior [c and d]). e and f, Snapshot of the tissue activated by 150 and 42 ms, respectively.

The bulk and bundle conductivities were set to produce local conduction velocities that were reasonable compared with experimental reports. With the assignment of only 3 conductivities, the global activation pattern could be analyzed. In subsequent text, comments are made regarding both the local conduction velocities and the global patterns of activation, and comparisons are made to experimental reports where such data are available.

Upon leaving the SA node, one pathway for the excitation wavefront in the model is along the crista terminalis in the posterior right atrial wall. Located at the intersection of the primitive atrium and sinus venosus, there is universal agreement that this prominent muscle bundle serves as a preferential pathway for atrial conduction.[4,27,44,45] Boineau et al[46] have presented mapping data from normal sinus in humans. The influence of the crista is visible in their data as a deflection in the isolines in the posterior right atrium and in the simulation in Figure 5 (especially panels a through c). The deflection is equally as obvious in maps of human right atrial activation published by Durrer et al.[4] Measures of the conduction velocity in this structure (all from canine studies, perhaps owing to the difficulty of making this measurement in humans) have varied widely. A reasonable average, however, is 70 to 130 cm/s.[44] The values in the model, between ≈110 cm/s and 134 cm/s, fall within this range. It is interesting to note that the distal value of conduction velocity is notably smaller than the proximal one. A possible explanation for this slowing of the wavefront is that, as the wave advances, it becomes progressively more curved in nature and must excite a greater amount of surrounding tissue.[47]

An alternative exit from the SA node is into the surrounding free wall.[46] This region, thin compared with the more substantial bundles characteristic of the right atrium,[16] is assigned an isotropic conductivity in the model. An excitation wavefront nearly that is devoid of local deviation results. This pattern compares favorably with the Durrer et al[4] data and the

isolines in maps published by Boineau et al[46] in which no preferential routes are evident within the free wall (except as noted below). A typical value for the simulated conduction velocity in the free wall is 74.6 cm/s. This number is within the range of 68 to 103 cm/s recently reported by Hansson et al.[48]

Moreover, in that study, these researchers observed no directional difference in mean conduction velocity, supporting the isotropic assumption in the free wall of our model. Similarly, Gray et al[16] reported an anisotropic ratio of nearly 1.0 in the sheep epicardial free wall, except at high pacing rates. The simulated free wall conduction velocity was subject to local variations. At a point of junction between an underlying pectinate muscle and the epicardial layer, for instance, it increased to a value of 95.4 cm/s. These variations have been reported in canine free wall measurements, where Wu et al[17] have attributed such nonuniformities to the presence of gross endocardial structures such as pectinates.

Reported times for total activation of the right atrial free wall vary. Canavan et al[59] indicate a duration of just >80 ms. Other studies, however, assert a time between 70 and 80 ms[49] or ≈60 ms.[46] The corresponding value for our model is ≈60 ms.

The conduction of the atrial impulse from the crista terminalis to the pectinate muscles is hidden from the epicardial views in published maps of human activation.[46] In the model, the conduction velocities in the free-running portion of the pectinates are ≈160 cm/s. Waves may also travel transversely between the pectinates at, for example, ≈116 cm/s. Compare these speeds with the canine pectinate velocities of between 117 and 154 cm/s reported by Hayashi et al.[42] The numbers cited by Spach et al in adult humans, between 58 to 78 cm/s for longitudinal conduction, are considerably lower. These velocities, however, were recorded subsequent to point stimulation. The resulting curved wavefront would be expected to propagate more slowly than the essentially planar waves existing in the pectinates during a normal sinus rhythm.[47] It is worthy to note, in the model, the typically faster conduction velocities in the pectinate muscles compared with the crista terminalis, in spite of the assignment of the same longitudinal conductivities within these structures. The source of this disparity is found in the different environments of the 2 bundles; whereas the pectinates are largely free-running, the crista velocity is slowed by the surrounding electrically coupled tissue.

The modeled pectinate muscles are mostly discontinuous[50]; the underlying endocardial surface is coupled to them at only one place during their length and at their ends. This anatomy, similar to that reported by Schuessler et al,[50] gives rise to a difference in epicardial-endocardial conduction time (in particular, see Figure 6b) as the fast conduction in the pectinates precedes that of the overlying wall. This phenomenon of discordant epicardial-to-endocardial activation is the major result of the Schuessler et al study. In the model, the fast activation of the pectinates causes a region of breakthrough near the tip of the right atrial appendage. Jalife and Gray[51] comment on a similar breakthrough pattern in the appendage in their studies with sheep.

The last pathway out of the SA node is via the arch of the crista, a structure in which modeled conduction proceeds at ≈122 cm/s. This route brings the wavefront to the interatrial septum. Alternatively, the wavefront can reach this region by traveling down the crista and across the intercaval bundle or through the adjacent venous tissue (in the newborn, at least[1]). Experimental reports of activation in the right atrial septum have shown diverse patterns in mapped human patients. In one study in humans,[52] the authors comment on the rapid spread of activation in the thick bundles of the septum, especially the anterior limbus of the oval fossa. These results are in agreement with an earlier report by Spach et al[1] performed in dogs and rabbits. In that study, the authors assert that the patterns of septal conduction are, in large part, a simple consequence of the anatomy of the bundles contained therein.[1] These observations are manifest, as well, in our modeled septal activation. The excitation impulse arrives at the septum as 2 waves. Within it, the wavefront is deformed when it reaches the fossa ovalis rim, where it travels at ≈115 cm/s. In other regions in the septum, far from wavefront collision, the wave velocity averages ≈76 cm/s. These velocities may be compared with a mean value of right atrial septal conduction velocity of 98 cm/s measured during electrophysiological study in 21 normal patients.[34] Canavan et al[59] report that the wavefront reaches the inferior atrial septum below the coronary sinus 85 ms after beat initiation. In the model, the point just distal to the coronary sinus in the direction of wave propagation is activated at 88 ms.

The crista terminalis, at its end, ramifies the floor of the right atrium. Within this region is located the so-called ''isthmus'' of slow conduction,[26,53,54] commonly considered to be bounded by the tricuspid annulus, the os of the coronary sinus, and the inferior vena cava. Modeled conduction is slow in this isthmus, declining to a velocity of ≈40 cm/s. Experimental reports of this measure are quite variable. In 17 patients with symptomatic typical atrial flutter, the mean conduction velocities in the isthmus were 60 cm/s, which was slower than the velocities measured in other limbs of the flutter circuit (≈100 cm/s).[55] A later study reports velocities of 83 to 89 cm/s in healthy patients but only 39 to 46 cm/s in patients predisposed to flutter.[34] The authors conclude that the slow isthmus conduction is an important contributor to isthmus-dependent atrial flutter. In 1997, Feld et al[36] reported similar numbers (50 to 55 cm/s in patients without flutter, 37 to 42 cm/s in patients with flutter). The conduction velocities in the modeled isthmus are consistent with those healthy patients at greater risk for flutter; when the bulk conductivity value was assigned to this region, however, the time for total right atrial activation decreased from 99.3 to 81.2 ms.

One of the pathways for interatrial connection is via Bachmann's bundle. The modeled interatrial conduction velocity within this structure is quite rapid, ≈177 cm/s. At the junction with the left atrial wall, however, the speed slows considerably, to ≈50 cm/s. This deceleration occurs as the impulse undergoes a dramatic shift in fiber direction and an increase in electrical load. It then accelerates back to a value of ≈117 cm/s within the left atrial wall. That Bachmann's bundle is a region of fast conduction is not in dispute.[42,43,56] Hayashi et al[42] measured the conduction velocity of Bachmann's bundle in dogs at 166 cm/s. Dolber and Spach[43] reported values for longitudinal conduction within the adult dog of 92 to 167 cm/s. In the model, Figure 6c shows the

elliptical spread of electrical activation due to rapid spread in Bachmann's bundle. The work of Hayashi et al[42] contains an illustration of the activation sequence in which the isolines are similarly displaced.

Bachmann's bundle represents one of the two interatrial connections implemented in the model. The other is located in the region of the fossa ovalis.[57,58] Activation of the septa of the right and left atria has been described as discordant,[37] perhaps a reflection of a layer of connective tissue contained therein.[52] Schuessler et al[38] reported, in dogs, that the left atrial septum consistently activated 10 ms later than the right. In recognition of this reality, the fossa ovalis interatrial connection was assigned the slow conductivity value. The modeled wave takes ≈12 ms to traverse this structure. Breakthrough on the left atrial septum occurs in the model in 2 places (Figure 8b), and wavefront progression is primarily superior to inferior. Both of these observations are also made by Sun et al,[37] in their simultaneous study of the canine right and left septa. Recently, a third interatrial connection has been suggested in the region of the coronary sinus.[57,58] No attempt was made to include this connection in the model.

Within the left atrium, modeled conduction completely engulfs the appendage at ≈88 ms. Ultimately, the region of last activation within the atria occurs in the lateral posterior region, at 108.2 ms. The activation pattern in the data of Boineau et al[46] is similar. There, the excitation wave reaches the appendage tip between 80 and 90 ms. Later, 2 waves converge in the posterior lateral region, colliding soon after 110 ms. This time of last activation is by all accounts variable. Lin et al[34] report P-wave durations of 114 ms among 21 healthy patients. Canavan et al[59] presented a map of human data where last activation occurred just after 120 ms. These authors also point out that in the studies of Durrer et al,[4] the region of last activation mentioned was within the left atrial appendage. The reason for the discrepancy with their work, they assert, is that the posterior left atrium was incompletely mapped in Durrer et al's preparation. Spach et al[3] in 1971 also found that the last region to depolarize is in the inferior-lateral left atrial wall. At the last region of activation in Boineau et al's maps,[46] 2 wavefronts may be observed converging. This contrasts with the simulated activity, in which 3 wavefronts come together at this last point. This discrepancy may be accounted for by recognizing that the third wavefront in the simulation, not observed in the experimental figure, approaches the tissue from the region between the pulmonary veins, a region that could not be mapped. Finally, the models of paced activity showed a relative lengthening of activation when the stimulus was placed at the left, versus the right, appendage. This feature is also present in the report by Boineau et al.[46] Further comments on these patterns are made by Harrild.[60]

Limitations

Our model, as described, represents the product of a great number of tradeoffs and simplifying assumptions. Many anatomical features could be captured more realistically in future models. The pectinate muscles, for example, could have more branches and transverse connections. Also, the thickness of the walls could vary more realistically in the present model, where the left and right atria have relatively uniform thicknesses (3 and 2 mm, respectively). The impact of greater variation in wall thickness on global activation is expected to be small, but this requires further study. The atrial mesh also does not include a recently described electrical connection at the coronary sinus.[57]

Another limitation involves the model discretization. Relatively large elements have been used to keep the simulations tractable. Because the Nygren et al[18] model gives rise to an action potential with a relatively slow upstroke, the resulting conduction velocities are less sensitive to the discretization than those obtained from a model with a faster depolarization phase. To obtain reasonable velocities with the dynamics of the Nygren et al[18] model, however, relatively large conductivities are needed. Although an atrial membrane model with a faster upstroke, such as the one described by Courtemanche et al,[61] would produce equivalent conduction velocities using lower conductivities, a finer overall spatial and temporal discretization would be required to capture the faster dynamics and sharper spatial fronts. The implication of using a finer discretization is significant. Recall that in 3 dimensions, simply halving the element sizes will lead to an 8-fold increase in the number of grid points, significantly increasing the simulation times and required computational resources. Even with a more refined model, however, we would expect the same overall patterns of activation, assuming no significant source to load differences in normal tissue. The impact of the element sizes is expected be greater when attempting to simulate conditions of disease or aging.

Finally, the present model uses uniform conductivities and a monodomain formulation rather than attempting to represent accurately connections at the cellular level. For example, in reality, the crista is coupled in a complex fashion to the SA node. Although the overall patterns of crista activation are consistent with gross measurements, clearly, the fine details depend on the microstructure. The additional complexity provided by this discreteness may be critical to the origin of some arrhythmias. Although the finite volume formation can incorporate some level of this discreteness, a proper treatment of activity at the cellular scale would require a model with >200 million elements. To make such a solution tractable, advances in either computer hardware or space/time adaptive algorithms will be necessary.[62]

Acknowledgments

This work was supported by NSF ERC Grant CDR-8622201, a grant of supercomputer time from the North Carolina Supercomputing Center, National Institutes of Health (NIH)/NIGMS Medical Scientist Training Program Grant GM-07171, NSF Grant DBI 9974533, and NIH Grant R29-HL57473.

References

1. Spach MS, Lieberman M, Scott JG, Barr RC, Johnson EA, Kootsey JM. Excitation sequences of the atrial septum and the AV node in isolated hearts of the dog and rabbit. *Circ Res.* 1971;29:156–172.
2. Lewis T, Meakins J, White P. Excitatory process in the dog's heart, I: the auricles. *Philos T Roy Soc B.* 1914;205:275–420.
3. Spach MS, King TD, Barr RC, Boaz DE, Morrow MN, Herman-Giddens S. Electrical potential distribution surrounding the atria during depolarization and repolarization in the dog. *Circ Res.* 1969;24:857–873.

4. Durrer D, van Dam RT, Freud GE, Janse MU, Meijler FL, Arzbaecher RC. Total excitation of the isolated human heart. *Circulation*. 1970;41: 899–912.
5. Boineau JP, Schuessler RB, Mooney CR, Miller CB, Wylds AC, Hudson RD, Borremans JM, Brockus CW. Natural and evoked atrial flutter due to circus movement in dogs: Role of abnormal atrial pathways, slow conduction, refractory period distribution and premature beats. *Am J Cardiol*. 1980;45:1167–1181.
6. Lesh MD, Kalman JM, Olgin JE, Ellis WS. The role of atrial anatomy in clinical atrial arrhythmias. *J Electrocardiol*. 1996;29:101–113.
7. Moe G, Rheinbold W, Abildskov J. A computer model of atrial fibrillation. *Am Heart J*. 1964;67:200–220.
8. Macchi E. Digital-computer simulation of the atrial electrical excitation cycle in man. *Adv Cardiol*. 1974;10:102–110.
9. Kafer CJ. Internodal pathways in the human atria: a model study. *Comput Biomed Res*. 1991;24:549–563.
10. Lorange M, Gulrajani RM. A computer heart model incorporating anisotropic propagation, I: model construction and simulation of normal activation. *J Electrocardiol*. 1993;26:245–260.
11. Wei D, Okazaki O, Harumi K, Harasawa E, Hosaka H. Comparative simulation of excitation and body surface electrocardiogram with isotropic and anisotropic computer heart models. *IEEE Trans Biomed Eng*. 1995;42:343–357.
12. Killmann R, Wach P, Dienstl F. Three-dimensional computer model of the entire human heart for simulation of reentry and tachycardia: gap phenomenon and Wolff-Parkinson-White syndrome. *Basic Res Cardiol*. 1991;86:485–501.
13. Earm YE, Noble D. A model of the single atrial cell: relation between calcium current and calcium release. *Proc R Soc Lond B Biol Sci*. 1990;240:83–96.
14. Virag N, Blanc O, Vesin JM, Koerfer J, Kappenberger L. Anatomical model of atrial arrhythmias. In: *International Workshop on Computer Simulation and Experimental Assessment of Electrical Cardiac Function*. 1998:91–95.
15. Luo CH, Rudy Y. A model of the ventricular cardiac action potential. Depolarization, repolarization, and their interaction. *Circ Res*. 1991;68: 1501–1526.
16. Gray RA, Pertsov AM, Jalife J. Incomplete reentry and epicardial breakthrough patterns during atrial fibrillation in the sheep heart. *Circulation*. 1996;94:2649–2661.
17. Wu TJ, Yashima M, Xie F, Athill CA, Kim YH, Fishbein MC, Qu Z, Garfinkel A, Weiss JN, Karagueuzian HS, Chen RS. Role of pectinate muscle bundles in the generation and maintenance of intra-atrial reentry: potential implications for the mechanism of conversion between atrial fibrillation and atrial flutter. *Circ Res*. 1998;83:448–462.
18. Nygren A, Fiset C, Firek L, Clark JW, Lindblad DS, Clark RB, Giles WR. Mathematical model of an adult human atrial cell. The role of K^+ currents in repolarization. *Circ Res*. 1998;82:63–81.
19. Rodefeld MD, Branham BH, Schuessler RB, Hand DE, Gamache CM, Platt JW, Labarbera SP, Cox JL, Boineau JP. Global electrophysiological mapping of the atrium: computerized three-dimensional mapping system. *Pacing Clin Electrophysiol*. 1997;20:2227–2236.
20. Cohen GI, White M, Sochowski RA, Klein AZ, Bridge PD, Stewart WJ, Chan KL. Reference values for normal adult transesophageal echocardiographic measurements. *J Am Soc Echocardiogr*. 1995;8:221–230.
21. Sunderman W, Boerner F. Anatomical normals. In: *Normal Values in Clinical Medicine*. Philadelphia, Pa: WB Saunders Co; 1949.
22. Coffey JL, Cristy M, Warner GG. Specific absorbed fractions for photon sources uniformly distributed in the heart chambers and heart wall of a heterogeneous phantom. *J Nucl Med*. 1981;22:65–71.
23. Bommer W, Weinert L, Neumann A, Neef J, Mason D, DeMaria A. Determination of right atrial and right ventricular size by two-dimensional echocardiography. *Circulation*. 1979;60:91–100.
24. Hiraoka A, Karakawa S, Yamagata T, Matsuura H, Kajiyama G. Structural characteristics of Koch's triangle in patients with atrioventricular node reentrant tachycardia. *Hiroshima J Med Sci*. 1998;47:7–15.
25. Kitzman DW, Scholz DG, Hagen PT, Ilstrup DM, Edwards WD. Age-related changes in normal human hearts during the first 10 decades of life, II (maturity): a quantitative anatomic study of 765 specimens from subjects 20 to 99 years old. *Mayo Clin Proc*. 1988;63:137–146.
26. Cabrera JA, Sanchez-Quintana D, Ho SY, Medina A, Anderson RH. The architecture of the atrial musculature between the orifice of the inferior caval vein and the tricuspid valve: the anatomy of the isthmus. *J Cardiovasc Electrophysiol*. 1998;11:1186–1195.
27. Wang K, Ho SY, Gibson DG, Anderson RH. Architecture of atrial musculature in humans. *Br Heart J*. 1995;73:559–565.
28. Callans DJ, Schwartzman D, Gottlieb CD, Marchlinski FE. Insights into the electrophysiology of atrial arrhythmias gained by the catheter ablation experience: "learning while burning, part II." *J Cardiovasc Electrophysiol*. 1995;6:229–243.
29. Moreno FL, Hagan AD, Holmen JR, Pryor TA, Strickland RD, Castle CH. Evaluation of size and dynamics of the inferior vena cava as an index of right-sided cardiac function. *Am J Cardiol*. 1984;53:579–585.
30. Papez JW. Heart musculature of the atria. *Am J Anat*. 1920;27:255–277.
31. Weatherill NP. Grid generation: structured, unstructured, or both? In: Stow P, ed. *Computational Methods in Aeronautical Fluid Dynamics*. Oxford, England: Clarendon Press; 1990:345–365.
32. Thompson JF, Weatherill NP. Structured and unstructured grid generation. *Crit Rev Biomed Eng*. 1992;20:73–120.
33. Harrild DM, Penland RC, Henriquez CS. A flexible method for simulating cardiac conduction in three-dimensional complex geometries. *J Electrocardiol*. 2000;33:241–251.
34. Lin JL, Lai LP, Lin LI, Tseng YZ, Lien WD, Huang SK. Electrophysiological determinant for induction of isthmus dependent counterclockwise and clockwise atrial flutter in humans. *Heart*. 1999;81:73–81.
35. Takahashi A, Shah DC, Jais P, Hocini M, Clementy J, Haissaguerre M. Partial cavotricuspid isthmus block before ablation in patients with typical atrial flutter. *J Am Coll Cardiol*. 1999;33:1996–2002.
36. Feld GK, Mollerus M, Birgersdotter-Green U, Fujimura O, Bahnson TD, Boyce K, Rahme M. Conduction velocity in the tricuspid valve-inferior vena cava isthmus is slower in patients with type I atrial flutter compared to those without a history of atrial flutter. *J Cardiovasc Electrophysiol*. 1997;8:1338–1348.
37. Sun H, Velipasaoglu EO, Wu DE, Kopelen HA, Zoghbi WA, Spencer WA III, Khoury DS. Simultaneous multisite mapping of the right and the left atrial septum in the canine intact beating heart. *Circulation*. 1999; 100:312–319.
38. Schuessler RB, Boineau JP, Bromberg BI, Hand DE, Yamauchi S, Co JL. Normal and abnormal activation of the atrium. In: Zipes D, Jalife J, eds. *Cardiac Electrophysiology: From Cell to Bedside*. Philadelphia, Pa: WB Saunders Co; 1995:367–380.
39. Plonsey R, Barr RC. *Bioelectricity: A Quantitative Approach*. New York, NY: Plenum Press; 1988.
40. Spach MS, Miller WT III, Barr RC, Geselowitz DB. Electrophysiology of the internodal pathways: determining the difference between anisotropic cardiac muscle and a specialized tract system. In: Little R, ed. *Physiology of Atrial Pacemakers and Conductive Tissue*. Armonk, NY: Futura Publishing Co; 1980:367–380.
41. Ho SY, Sanchez-Quintana D, Anderson RH. Can anatomy define electric pathways? In: *International Workshop on Computer Simulation and Experimental Assessment of Electrical Cardiac Function*. 1998:77–86.
42. Hayashi H, Lux R, Wyatt R, Burgess MJ, Abildskov JA. Relation of canine atrial activation sequence to anatomic landmarks. *Am J Physiol*. 1982;242:H421–H428.
43. Dolber PC, Spach MS. Structure of Bachmann's bundle related to propagation of excitation. *Am J Physiol*. 1989;257:H1446–H1457.
44. Boineau JP. Atrial flutter: a synthesis of concepts. *Circulation*. 1985;72: 249–257.
45. Spach MS, Miller WT III, Dolber PC, Kootsey JM, Sommer JR, Mosher CE Jr. The functional role of structural complexities in the propagation of depolarization in the atrium of the dog: cardiac conduction disturbances due to discontinuities of effective axial resistivity. *Circ Res*. 1982;50: 175–191.
46. Boineau JP, Canavan TE, Schuessler RB, Cain ME, Corr PB, Cox JL. Demonstration of a widely distributed atrial pacemaker complex in the human heart. *Circulation*. 1988;77:1221–1237.
47. Cabo C, Pertzov AM, Baxter WT, Davidenko JM, Gray RA, Jalife J. Wave-front curvature as a cause of slow conduction and block in isolated cardiac muscle. *Circ Res*. 1994;75:1014–1028.
48. Hansson A, Holm M, Blomstrom P, Johansson R, Luhrs C, Brandt J, Olsson S. Right atrial free wall conduction velocity and degree of anisotropy in patients with stable sinus rhythm studied during open heart surgery. *Eur Heart J*. 1998;19:293–300.
49. Cox JL, Canavan TE, Schuessler RB, Cain ME, Lindsay BD, Stone C, Smith PK, Corr PB, Boineau JP. The surgical treatment of atrial fibrillation, II: intraoperative electrophysiological mapping and description of the electrophysiologic basis of atrial flutter and atrial fibrillation. *J Thorac Cardiovasc Surg*. 1991;101:406–426.

50. Schuessler RB, Kawamoto T, Hand DW, Mitsuno M, Bromburg B, Cox JL, Boineau JP. Simultaneous epicardial and endocardial activation sequence mapping in the isolated canine right atrium. *Circulation*. 1993; 88:250–263.
51. Jalife J, Gray RA. Insights into the mechanisms of atrial fibrillation: role of the multidimensional atrial structure. In: Murgatroyd FD, Camm AJ, eds. *Nonpharmacological Management of Atrial Fibrillation*. Armonk, NY: Futura Publishing Co, Inc.; 1997:357–377.
52. Chang BC, Schuessler RB, Stone CM, Branham BH, Canavan TE, Boineau JP, Cain ME, Corr PB, Cox JL. Computerized activation sequence mapping of the human atrial septum. *Ann Thorac Surg*. 1990; 49:231–241.
53. Schoels W, Kubler W, Yang H, Gough WB, El-Sherif N. A unified functional/anatomic substrate for circus movement atrial flutter: activation and refractory patterns in the canine right atrial enlargement model. *J Am Coll Cardiol*. 1993;21:73–84.
54. Cosio FG, Arribas F, Lopez-Gil M, Palacios J. Atrial flutter mapping and ablation, I: studying atrial flutter mechanisms by mapping and entrainment. *Pacing Clin Electrophysiol*. 1996;19:841–853.
55. Shah DL, Jais P, Haissaguerre M, Chouairi S, Takahashi A, Hocini M, Garrigue S, Clementy J. Three-dimensional mapping of the common atrial flutter circuit in the right atrium. *Circulation*. 1997;96:3904–3912.
56. Bachmann G. The inter-auricular time interval. *Am J Physiol*. 1916;41: 309–320.
57. Antz M, Otomo K, Arruda M, Scherlag BJ, Pitha J, Tondo C, Lazzara R, Jackman WM. Electrical conduction between the right atrium and the left atrium via the musculature of the coronary sinus. *Circulation*. 1998;98:1790–1795.
58. Roithinger FX, Cheng J, Sippens Groenewegen A, Lee R, Saxon L, Scheinman M, Lesh M. Use of electroanatomic mapping to delineate transseptal atrial conduction in humans. *Circulation*. 1999;100: 1791–1797.
59. Canavan TE, Schuessler RB, Boineau JP, Corr PB, Cain ME, Cox JL. Computerized global electrophysiological mapping of the atrium in patients with Wolff-Parkinson-White syndrome. *Ann Thorac Surg*. 1988; 46:223–231.
60. Harrild DM. *Why Anatomy Matters: Normal Conduction and Flutter in a Computer Model of the Human Atria* [dissertation]. Durham, NC: Duke University; 2000.
61. Courtemanche M, Ramirez RJ, Nattel S. Ionic mechanisms underlying human atrial action potential properties: insights from a mathematical model. *Am J Physiol*. 1998;275(1 pt 2):H301–H321.
62. Cherry EM, Greenside HS, Henriquez CS. A space-time adaptive method for simulating complex cardiac dynamics. *Physiol Rev Lett*. 2000;84: 1343–1348.